SEARS
Ship Emissions to Atmosphere
Reporting Service
Contract No. 400104295

D3 – Assessing the potential of satellite instruments to detect and quantify SO_2 from ships

Reference: SEARS_D3_detection_of_SO_2
Issue 1.0
Date: July 2014
Prepared for: ESA

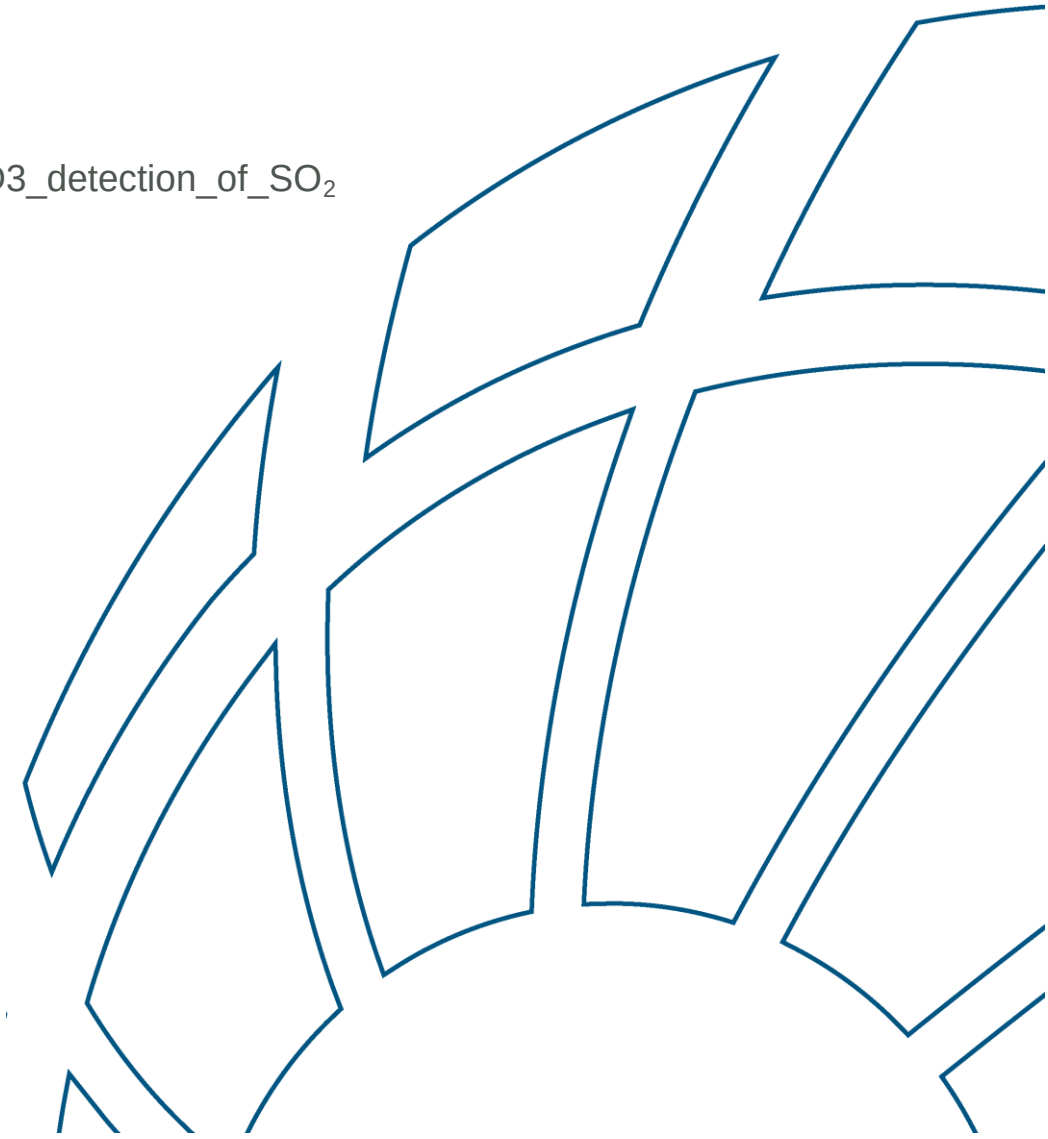

Document status sheet

Title	: D3 – Assessing the potential of satellite instruments to detect and quantify SO_2 from ships
Code	: SEARS-D3
Date	: July 2014
Status	: Final
Issue	: 1.0
Contractnr	: 4000104295/11/I-NB
Projectnr	: A11025
Project name	: SEARS
Prepared for	: ESA
Author(s)	: Andreas Richter (IUP) Andreas Hilboll (IUP) Huan Yu (BIRA) Michel van Roozendael (BIRA) Isabelle de Smedt (BIRA) Gerard Hesselmans (HERMESS) Agnes Mika (BMT ARGOSS)
Approved by	: Hein Zelle (BMT ARGOSS)
Distribution	: ESA EMSA BMT ARGOSS IUP BIRA HERMESS

Contents

List of abbreviations and acronyms

AMF	Air Mass Factor
BIRA	Belgian Institute for Space Aeronomy
CF	Cloud Fraction
CTM	Chemistry-Transport Model
CHIMERE	Regional chemistry-transport model
DOAS	Differential Optical Absorption Spectroscopy
ECMWF	European Centres for Medium-range Weather Forecasts
GOME-2	Global Ozone Monitoring Experiment-2
IUP	Institute of Environmental Physics (University of Bremen)
KNMI	Dutch Royal Meteorological Institute
LER	Lambertian Equivalent Reflectance
MODIS	Moderate Resolution Imaging Spectroradiometer
OMI	Ozone Monitoring Instrument
PBL	Planetary Boundary Layer (name of OMI SO_2 product)
RTM	Radiative Transfer Model
STL	Standard Layer (name of OMI SO_2 product)
S4	Sentinel-4
S5P	Sentinel-5 Precursor
SCD	Slant Column Density
SNR	Signal-to-noise ratio
STD	STandard Deviation
SZA	Solar Zenith Angle
TROPOMI	TROPOspheric Monitoring Instrument
VCD	Vertical Column Density
WRF	Weather Research and Forecasting model

1. Introduction

Land-based emissions of SO_2 have been decreasing significantly over the last two decades in most industrialised countries, mainly because of implementation of desulphurisation technologies in power plants and switching to cleaner fuels. As a result, environmental problems from SO_2 pollution have decreased in these countries. At the same time, SO_2 emissions in China and India have been increasing as coal consumption for energy production as well as industrial applications has increased. Notably in China, a clear reduction has been achieved since 2006, again through implementation of desulphurisation in power plants.

However, SO_2 emissions from ships have not been regulated to a similar degree, and many ocean going ships use bunker oil with high sulphur content. With continuously increasing shipping volume, SO_2 emissions from ships have the potential to become the dominant SO_2 source not only in marine areas but also in coastal regions, where ship emissions are an important contribution to air quality problems. In response to this problem, sulphur emission control areas (SECAs) have been created first in 2000 for all European harbours, then in 2006 and 2007 for the Baltic Sea, the North Sea and the English Channel and in 2009 along the coast of California. In these regions, increasingly strict limits apply for the sulphur content of the fuel used. As low sulphur fuel is more expensive than bunker oil, there is a need to monitor compliance with the SECA rules, either by measurements of fuel sulphur content on board or of SO_2 emissions in the air, either by sniffing with in-situ instruments or by remote sensing.

Satellite observations in the UV from instruments such as TOMS, GOME, SCIAMACHY, OMI, and GOME-2 can be used to retrieve atmospheric columns of SO_2 with detection limits of about 1 DU depending on parameters such as surface reflectance and vertical SO_2 distribution. As result of increased Rayleigh scattering at short wavelengths, the sensitivity of SO_2 observations from space decreases strongly towards the surface, limiting the applicability to observation of pollution in the boundary layer. So far, no satellite based detection of SO_2 from ships has been reported in spite of clear detection of NO_2 in shipping lanes.

In this technical note, the potential of current satellite instrumentation to detect shipping SO_2 from space is evaluated and actions are discussed, which would make quantitative detection possible in the future.

2. Evaluation of expected SO_2 signal

2.1. Modelling set-up

The modelling set-up consists of a nested version of the CHIMERE chemistry and transport model coupled to WRF meteorology. Details on the model set-up including emission inventories and domain are given in Appendix A.

2.2. Modelled SO_2 vertical columns, diurnal variation, seasonality

Using the model output described above, tropospheric SO_2 columns were derived by vertically integrating the SO_2 profiles, averaging them over months and gridding them to a horizontal resolution of 0.125°. For this, only the model output for 04:00 UT was used as comparison of results for different times showed only small variations in the SO_2 column (see Figure 2.1).

The results are shown in Figure 2.1 where the spatial distribution of the SO_2 is shown for all months of the year. Several observations can be made from the model data

- There is a large seasonality in the SO_2 columns
- Only in some months, the shipping lane is clearly visible in the SO_2 maps while in others, the signal is more distributed as the result of strong winds
- The overall value of the SO_2 columns is small, of the order of 0.3 – 1.5x10^{15} molec cm^{-2} or 0.01 – 0.05 DU. Larger SO_2 columns are often observed over the adjacent land masses.

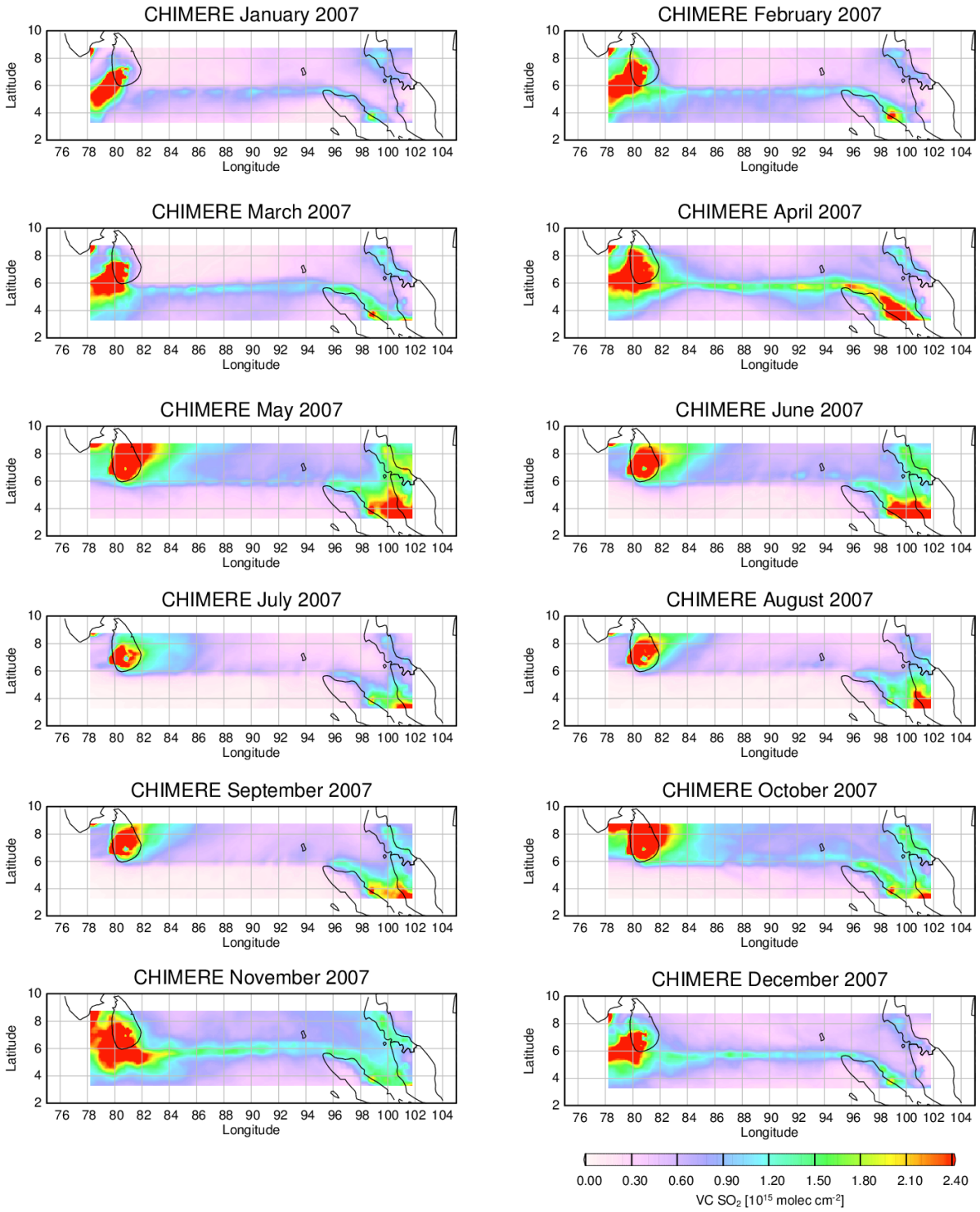

Figure 2.1: Monthly averages of modelled vertical columns of SO_2 for 2007

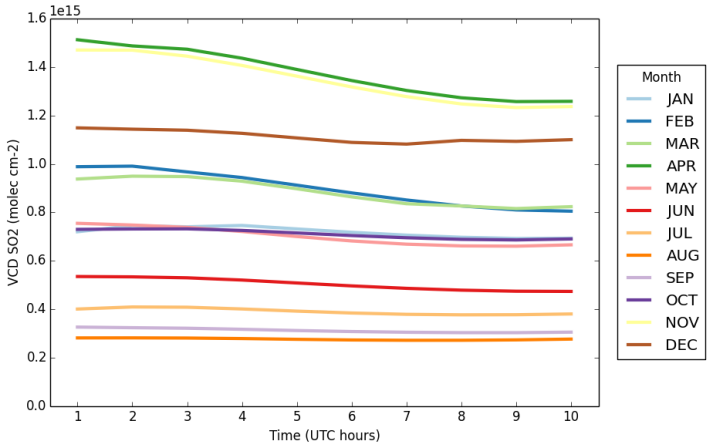

Figure 2.2: Temporal evolution of modelled shipping SO_2 in the Indian Ocean ship track for different months

In order to investigate the variation with local time, the SO_2 columns were integrated horizontally over the area 81° - 95°E, 5.35° - 5.95°N and the results plotted for different local times. As can be seen from Figure 2.2, changes over the relevant times are really small in all months with the exception of February, March, April, and November where they can be as large at 15%.

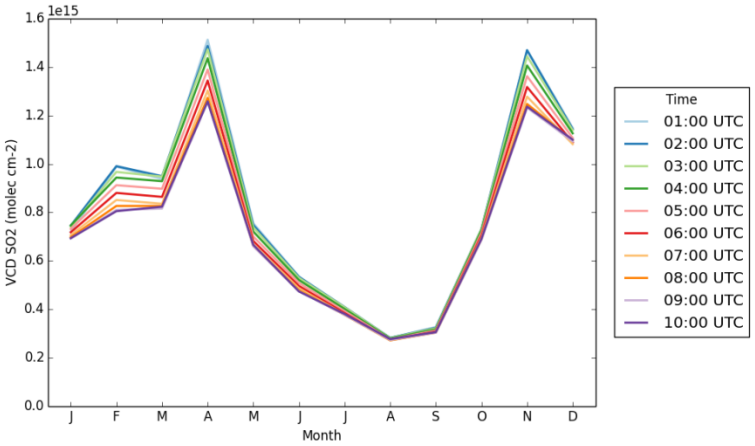

Figure 2.3: Seasonal variation of modelled shipping SO_2 in the Indian Ocean ship track for different months.

Another view of the same data is given in Figure 2.3, where the data are displayed as a function of month. The seasonal variation is large with a factor of more than 5 between August and April values. This variability is not the result of emission changes as little variation is expected in ship traffic over the year. It is rather driven by meteorology which determines both the atmospheric lifetime of SO_2 which is mainly limited by dry and wet deposition and the dilution which reduces SO_2 values at high wind speed.

While this result is strictly only valid for the year of simulations (2007), it is to be expected that it qualitatively also holds for other years. Any detection of shipping SO_2 in satellite data should therefore be easier in months with large and spatially well confined SO_2 columns.

2.3. Sensitivity of nadir satellite observations

In order to assess the signal that the satellite should see in the presence of the SO_2 distributions modelled by CHIMERE, the effect of radiative transfer needs to be considered. Here, the radiative transfer model SCIATRAN (Rozanov et al., 2014) was used to evaluate the sensitivity of the satellite observations to SO_2 and to create lookup tables for a fast conversion of the simulated vertical profiles to expected slant columns.

The sensitivity of UV/VIS nadir satellite measurements to SO_2 in the atmosphere depends on the vertical distribution of the SO_2, the viewing geometry, the surface reflectivity, the aerosol profile and the stratospheric O_3 column. As the retrieval of SO_2 is performed at short wavelengths, Rayleigh scattering is a large factor and most photons coming from the sun are scattered at least once before reaching the surface. As a result, the sensitivity to SO_2 absorption decreases strongly towards the surface as shown in Figure 2.4, top left for 4 wavelengths representative for the SO_2 fitting window typically used. As would be expected, there is some increase in sensitivity towards the larger wavelengths in the fitting window but that is not very pronounced. At the surface, sensitivity is very low (0.2) while at 10 km, it is about 2, approaching the geometric value of 2.3.

The SO_2 sensitivity in the lower troposphere depends on the surface reflectance, and increasing the value to 0.15 increases the box AMF for the lowest 2 kilometres by about a factor of 2 (Figure 2.4, top right).

In contrast to the situation for absorbers located in the stratosphere, the sensitivity to SO_2 in the troposphere does not depend strongly on solar zenith angle and only starts to decrease significantly at SZA larger than 70° (see Figure 2.4 bottom left).

Aerosols can have a large impact on the radiative transfer and the sensitivity of satellite observations. There are three counteracting effects – reducing the sensitivity to SO_2 below an aerosol layer (shielding effect), enhancing the sensitivity to SO_2 above an aerosol layer (albedo effect) and increasing the sensitivity to SO_2 within the aerosol layer (light path enhancement effect). If the aerosol is absorbing, both the albedo and light path enhancement effects are reduced. The overall impact on the signal depends critically on the relative vertical position of aerosol and SO_2. In the case of shipping emissions, two effects need to be considered. On the one hand, the natural sea salt aerosol which is reflective and situated very low in the atmosphere has an overall enhancing effect for shipping SO_2 with a small reduction close to the surface (see Figure 2.4 bottom right). On the other hand, ships also emit soot and other particles which at least close to the ships are at the same altitude as the shipping SO_2. This aerosol will probably reduce the sensitivity of the satellite measurements but depends on many parameters (fuel used, ship technology, atmospheric removal, etc.). This part of the aerosol effects was not considered here.

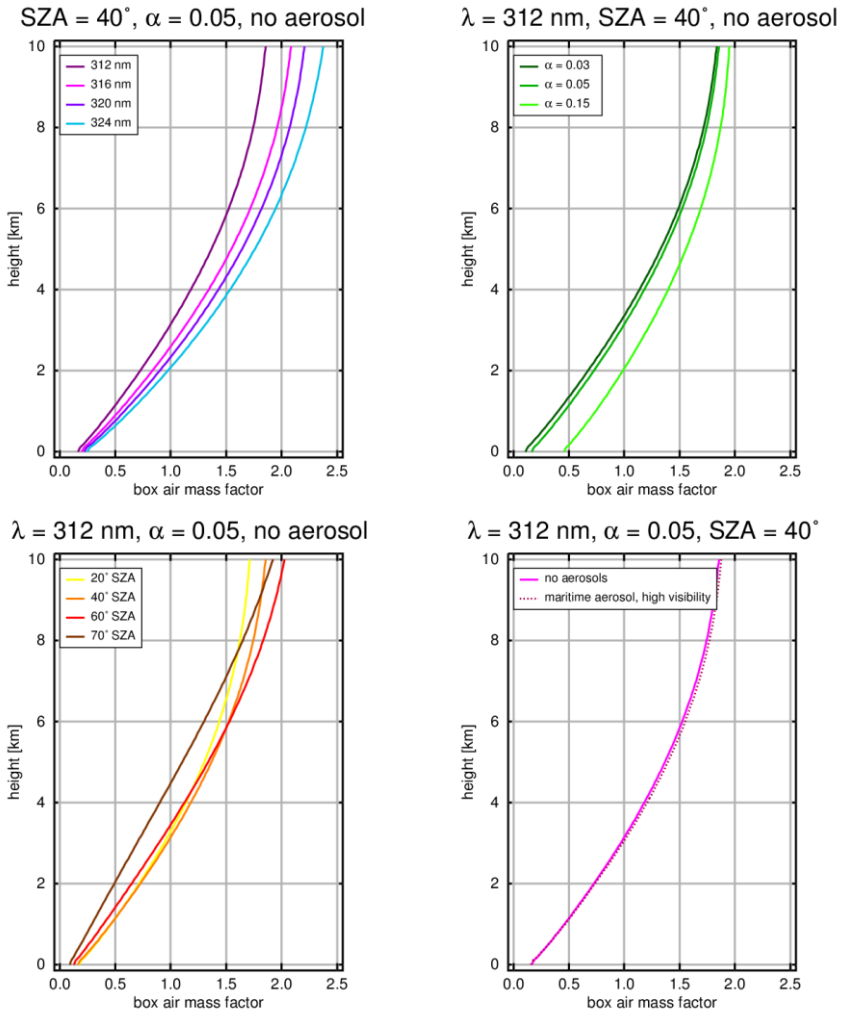

Figure 2.4: Evaluation of the vertical sensitivity (box air mass factor) for SO_2 comparing different wavelengths (top left), different surface reflectivity (top right), different solar zenith angles (bottom left) and the effect of a maritime aerosol (bottom right). In each figure, only one parameter is varied and the other settings are given in the header.

2.4. Modelled SO_2 slant columns, seasonality

In Figure 2.6, monthly averages of modelled slant columns are shown. Here, the nadir box AMFs for 312 nm, albedo 0.05 and a Rayleigh atmosphere as discussed in the previous section were applied to each model pixel by interpolating pre-calculated values onto the pressure levels of the model, multiplying with the partial SO_2 column and then integrating vertically to yield the slant column. The resulting AMFs have large horizontal and temporal variability as is illustrated in Figure 2.5 where the average AMF for the two extreme months of April and August are shown. As is to be expected, the AMF is lower where the SO_2 is close to the surface (in regions of emissions or downwind of such areas) and higher where the SO_2 is higher in the atmosphere (away from sources).

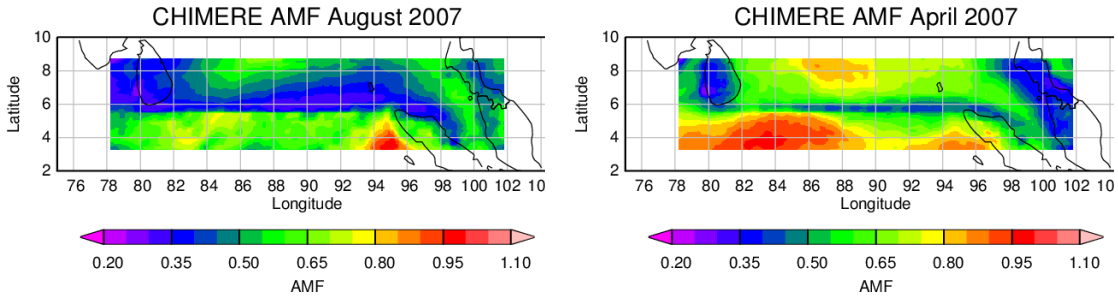

Figure 2.5: Monthly averages of air mass factors for SO_2 based on the CHIMERE vertical profiles and assuming a wavelength of 312 nm, 40° SZA, 0.05 albedo and a Rayleigh atmosphere.

Comparing slant and vertical SO_2 columns as shown in Figure 2.1 and Figure 2.6, two differences are apparent:

- The slant columns are smaller than the vertical columns by about a factor of two
- The contrast between the shipping lane and the rest of the region is reduced

Both effects the lower signal and the contrast reduction make detection of SO_2 shipping signals a challenge.

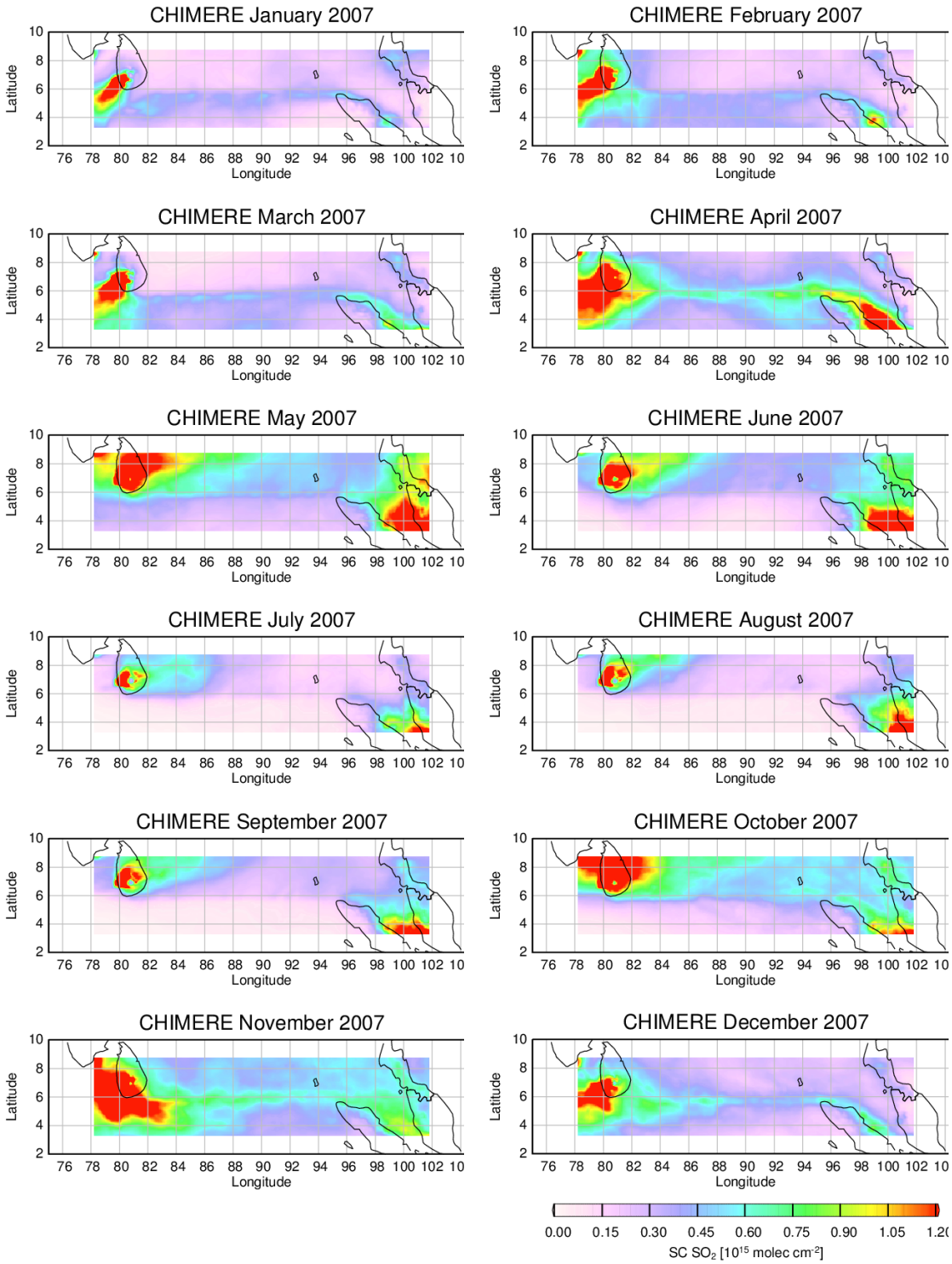

Figure 2.6: Monthly averages of modelled slant columns of SO_2 for 2007. For the AMF, an albedo of 0.05 was assumed, a solar zenith angle of 40° and a Rayleigh atmosphere. The AMF used is appropriate for 312 nm.

3. Evaluation of SO_2 products from current UV/VIS sensors

3.1. Approaches and limitations of current SO_2 products

All current SO_2 products from UV/vis satellite instruments use the differential absorption of SO_2 in the UV to detect SO_2 column amounts in the atmosphere. As SO_2 has a large and strongly structured absorption cross-section, it is relatively easy to detect and quantify using absorption spectroscopy. However, there are a number of problems complicating the SO_2 retrieval from satellite observations:

- As SO_2 absorbs in the UV, Rayleigh scattering is strong and the sensitivity to lower atmospheric layers is small
- As the sensitivity changes strongly with altitude and the vertical distribution of SO_2 cannot be retrieved from the measurements with the exception of elevated plumes coming from large volcanic eruptions, the a priori assumptions have a large impact on the quantitative results
- As many of the SO_2 sources are variable in space and time, the creation of good a priori data is much more difficult than for example for NO_2, leading to larger uncertainties and preventing cloud correction
- The total amount of ozone in the atmosphere has a significant impact on the SO_2 retrieval, both through spectral inteference and via changes of the AMF
- At large SO_2 amounts, the SO_2 can no longer be considered as a weak absorber, creating non-linearities in the absorption signal
- There are systematic biases and offsets in the SO_2 retrievals which are linked to ozone, clouds, bright surface and solar position.

As a result of these problems, all current SO_2 products rely on normalisation approaches to reduce artefacts from the retrievals. Also, it is usual to use simple a priori assumptions on the SO_2 profile, for example several different standard profiles for which results are provided. It is then in the responsibility of the user to select the most appropriate one for his / her application.

3.2. GOME-2

The IUP Bremen SO_2 product (A. Richter, 2009) includes the 312 nm band of SO_2 and therefore has relatively low noise. While this reduces the sensitivity to SO_2 close to the surface, experience shows that the increase in SO_2 cross-section more than offsets this disadvantage.

The iterative fitting applied in the IUP product for improved results in situations with large SO_2 content does not have any effect on the low values discussed here – all retrieval results are below the threshold for a second iteration. However, as vertical optical depths are fitted for SO_2, there is no slant column available but only the vertical columns based on the a priori used in the radiative transfer calculations. The corresponding AMF is roughly 2 for the region discussed here.

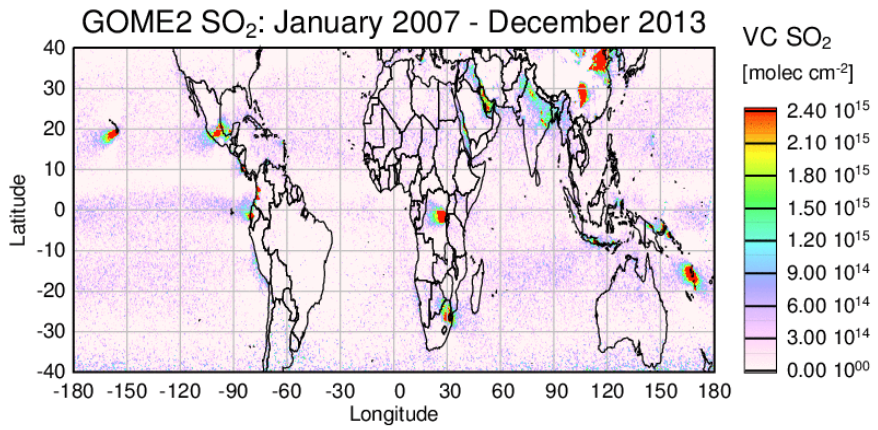

Figure 3.1: Long-term average of GOME-2 IUP vertical SO_2 columns. In this analysis, an AMF appropriate for volcanic signals was applied which will lead to underestimation in signals from pollution. Nevertheless, anthropogenic signals are evident in China, India, South Africa, and the Persian Gulf.

As shown in Figure 3.1, there are many SO_2 enhancements apparent in a global long term average of GOME-2 SO_2 data when using the same scale as used in Figure 2.1. However, there is no indication for SO_2 from the ship track between India and Indonesia.

As an additional test, an average was computed for the same time period but using only data with relatively small cloud contamination (FRESCO+ cloud fraction < 20%). In principle, lower cloud fractions improve detectability of pollution SO_2 which is situated close to the surface as clouds efficiently shield the lower troposphere from the satellite view. However, experience shows that in the case of SO_2, average signals are systematically lower in cloud screened data, probably because scenes having some SO_2 above clouds where it is well detectable contribute to the total average. At the same time, there are small but systematic biases between cloud screened and not cloud screened data in regions without SO_2 signal, presumably pointing at an interference from Raman scattering. As shown in Figure 3.2, the cloud screened data reveal as little evidence for shipping SO_2 as the original data set. However, the overall noise level is much increased as result of the rejection of a large number of observations.

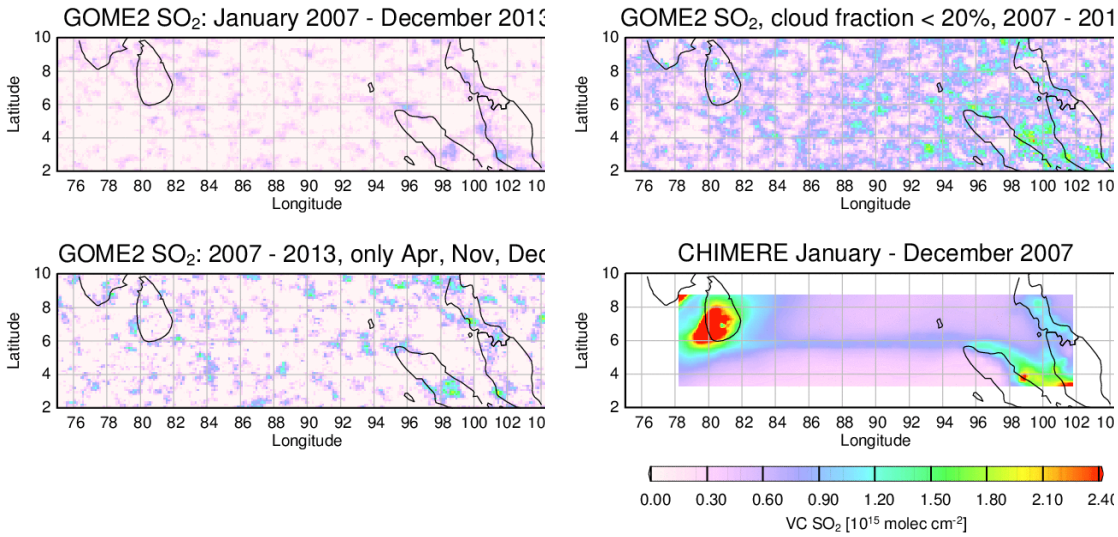

Figure 3.2: Comparison of three different long-term GOME2-2 SO_2 averages with CHIMERE data: Average over all data (top left), average over all data having less than 20% cloud fraction (top right) and average over April, November, and December only, those months having the highest shipping signals in the model. The AMF for GOME-2 data has not been corrected for BL SO2.

The modelled SO_2 columns show a large seasonal variation with much higher values in April, November and December than in other months. Therefore, a third average was computed without applying cloud screening but only including these three months of each year. As can be seen in Figure 3.2, also this average does not show evidence of a ship track and again has larger noise than the overall average as would be expected from the reduced number of measurements used (only one fourth).

It is interesting to also compare non shipping related SO_2 signals between model and measurements. Clearly, the model predicts much larger SO_2 over Madagascar and also three distinct hotspots in Indonesia and Malaysia. While there is no indication of elevated SO_2 over Madagascar in the GOME-2 data, the three SO_2 spots close to Medan in Indonesia and Kuala Lumpur in Malaysia appear to be also present in the satellite data, albeit at much lower intensity than in the model. These discrepancies can be linked to the use of a static inventory which uses long-term average values for volcanic emissions and anthropogenic emissions for the year 2007. It could on the other hand also be linked to the limited sensitivity of the satellite data set.

As discussed above, the AMF used in the GOME-2 product is appropriate for a volcanic plume, not BL pollution. Therefore, all SO_2 values should be multiplied by about 4 to account for the difference in AMF. By doing this, the spatial patterns shown in Figure 3.2 will not change (see discussion below). In order to further improve the signal to noise ratio, data along the ship track have been integrated to create a cross-section, both for the satellite data and the model values. The results are shown in Figure 3.3 with the AMF scaling of 4 applied. While there is a maximum in the satellite data at the right latitude and with similar amplitude as in the model data, there also are two smaller maxima at other latitudes which make this a less than unambiguous detection of shipping SO_2.

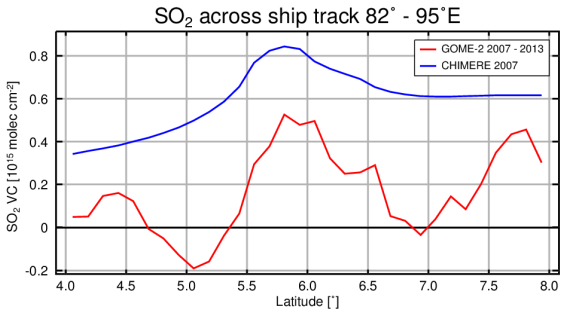

Figure 3.3: Cross section through the ship track between 82° and 95°E. GOME-2 data have been scaled by a factor of 4 to account for the difference in AMF between the standard product (AMF around 2) and the value appropriate for the shipping SO_2 (AMF around 0.5).

As can be seen from Figure 2.5, the AMF varies across the ship track and if applied properly, SO_2 values to the sides of the ship track would be reduced while they would increase in the centre. This would make the satellite data more similar to the model data and would better reflect the real situation. However, there is also a risk in applying this structured AMF to real data, as even a constant SO_2 field with nonzero values would lead to an apparent ship track in the data. This link between a priori, AMF and retrieved column over shipping regions is further discussed for NO_2 in Vinken et al., 2013.

The conclusion from the analysis of GOME-2 data is, that even in a long-term average from 2007 – 2013, there is no clear detection of the shipping SO_2 signal when integrating over the most busy shipping track of the world.

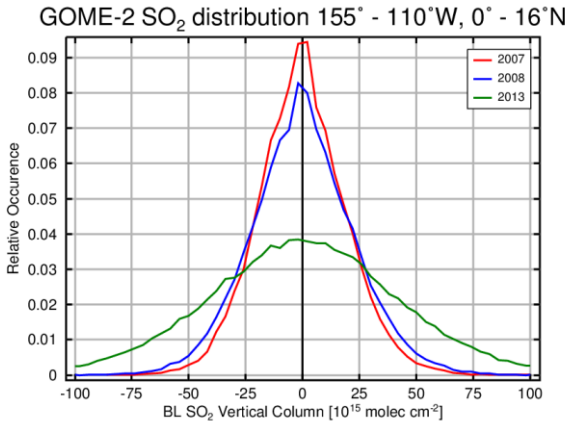

Figure 3.4: Distribution of GOME-2 SO_2 vertical columns over a clean region in the Pacific, where it is assumed that no SO_2 is present. The AMF used for this analysis is appropriate for shipping SO_2 (AMF = 0.5).

It is interesting to estimate the size of the smallest detectable SO_2 shipping signal from the scatter of the GOME-2 data. While the standard deviation of the data is not necessarily a good approximation of the detection limit, it can at least provide a lower estimate. In Figure 3.4, the distribution of SO_2 values retrieved in the month of April from GOME-2 data of the area (155 – 110°W, 0 – 16°N) is shown for different years assuming an AMF of 0.5. In 2007, the FWHM of the distribution is about 40×10^{15} molec cm^{-2} or 1.5 DU. Over the lifetime of GOME-2, it degrades to 88×10^{15} molec cm^{-2} (3.3 DU) as result of the throughput loss from instrument degradation. Assuming normal distribution of the values, the RMS can be reduced by averaging over time and space. The resulting values for some relevant scenarios are summarised in Table 1.

Table 1: Estimated GOME-2 SO_2 standard deviations for different scenarios. All values are given for an AMF of 0.5 and assume GOME-2 signal to noise from 2007.

Scenario	Number of values	σ [10^{15} molec cm^{-2}]	σ [DU]
Single Day	1	40	1.5
Month, all values	30	7.3	0.27
Month, clear-sky values	10	12.6	0.47
Year all values	365	2.1	0.078
7 years, all values	2555	0.8	0.029
7 years, all values, integrated along track	45990	0.2	0.007

Comparing the values in Table 1 with the range of shipping SO_2 values predicted by CHIMERE, and considering that only the enhancement relative to the background is detectable, it is clear, that only for the case with the strongest averaging (7 years, all values, integrated along the ship track between 82°E and 95°E) results in a standard deviation of 0.2x1015 molec cm-2 which is lower than the expected SO_2 contrast of about 0.4x1015 molec cm-2. Considering the degradation of GOME-2 SO_2 measurements over the time period averaged, it therefore cannot be expected to have a clear detection of shipping SO_2 in GOME-2 data. As shown in Figure 3.3, the results are however consistent with the columns modelled by CHIMERE.

3.3. OMI operational data

The operational NASA OMI SO2 product version 3 contains 4 different SO2 results. The PBL result which is intended for use with SO2 in the boundary layer is based on the band residual method and is computed during the OMI ozone retrieval. It assumes that all SO2 is in the PBL and that a constant AMF of 0.36 applies. No correction for clouds, albedo, aerosols or surface altitude is performed. The other three OMI SO2 products are intended for situations where the SO2 is at an elevated altitude. They are retrieved with the linear fitting retrieval and differ in the assumption on the vertical SO2 distribution. Here, we use the STL product to search for possible shipping signals in the data over the Indian Ocean.

From 2008 onwards, the row anomaly in the OMI instrument leads to loss of some viewing directions and larger uncertainties in others. While this has in part been corrected and flagged, there still is increased noise in the data from recent years. Therefore, averages over the first 4 years of OMI measurements (January 2005 – December 2008) are used here. In order to optimise the spatial resolution, the viewing directions having the largest pixels have not been included, limiting the data to rows 3 – 57.

Compared to GOME-2, the quality of an individual SO_2 retrieval from OMI is expected to be reduced as the ground pixel is much smaller (13 x 24 km^2 at nadir as compared to 40 x 80 km^2). However, the much larger number of observations can make up for this increased noise and in long-term averages, the SNR of OMI data should be superior to those of GOME-2. In addition, there is no strong degradation of the OMI instrument over time (with the exception of the row anomaly). Further improvements in OMI SO_2 SNR could result from application of a full DOAS retrieval to the spectra, but such a product is currently not available.

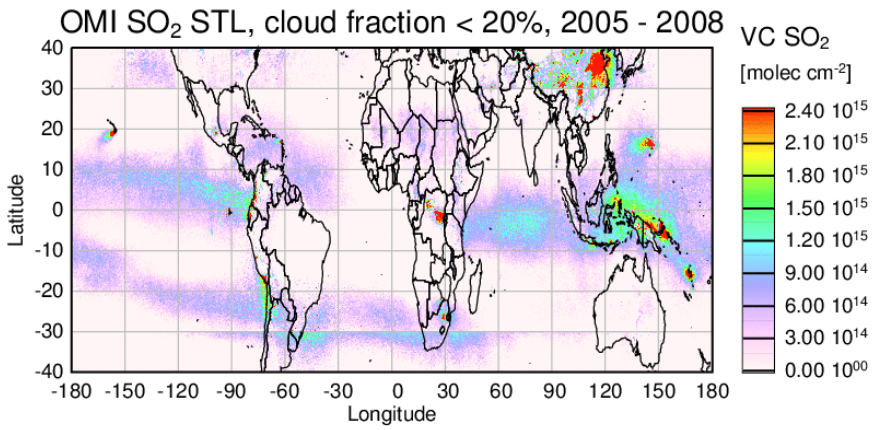

Figure 3.5: Long-term average of NASA OMI vertical SO_2 columns (STL product).

As shown in Figure 3.5, the overall pattern and values of the OMI STL product is comparable to that derived from GOME-2 (see Figure 3.1). Some differences are expected as the time period covered differs, and volcanic activity varies between years. At the same time, SO_2 signals over Asia have been increasing while SO_2 emissions in the US and Europe are decreasing.

As shown in Figure 3.6, OMI SO_2 data do not show any indication for the ship track between India and Indonesia. Also, the land based sources visible in CHIMERE data can hardly be identified, in line with the GOME-2 results shown in Figure 3.2. The noise of the data appears reduced in comparison to GOME-2 cloud screened data, but a large gradient is apparent with latitude. If no cloud screening is applied to the OMI data, SO_2 values decrease significantly and are negative for nearly the entire region shown in Figure 3.6. While a similar decrease is observed in GOME-2 data, the magnitude is much larger.

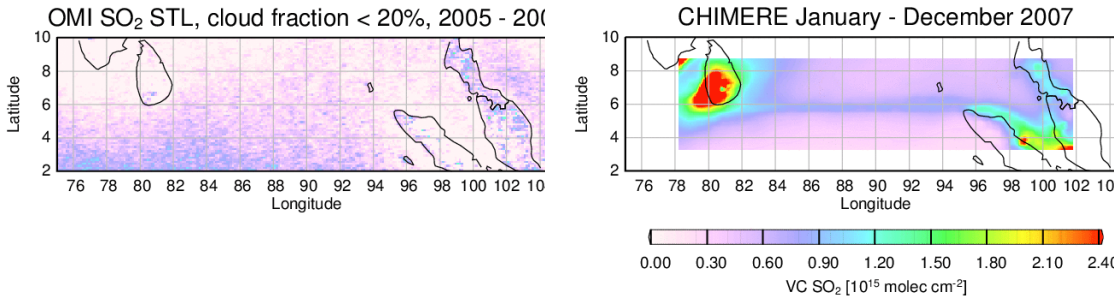

Figure 3.6: Comparison long-term OMI SO_2 (STL product) averages with CHIMERE data for 2007. A cloud threshold of 20% has been applied, and no correction of the AMF.

In Figure 3.7, cross-sections are shown for the entire ship track between 82° and 95°E. Three different OMI data sets are included – the average over all measurements, only observations having less than 20% cloud cover and values derived under sun glint conditions. The latter have not been cloud screened to increase the number of values. As for GOME-2, a rule of thumb correction (factor of 4) has been applied to account for the reduced sensitivity to SO_2 in the marine BL. The offset between the different data sets is obvious, indicating a cloud related bias in the OMI SO_2 product. After subtraction of a fitted straight line, the magnitude of the variations in SO_2 becomes similar between the different OMI evaluations and also the CHIMERE simulation, but in the satellite data, there is no indication of a shipping signal.

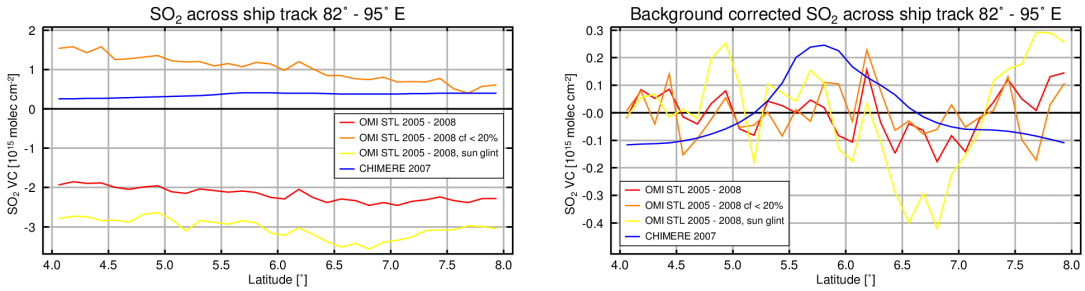

Figure 3.7: Cross section through the ship track between 82° and 95°E. OMI data have been scaled by a factor of 4 to account for the difference in AMF between the standard product and the value appropriate for the shipping SO_2. Left: absolute values, right: values after linear background correction.

The conclusion from the analysis of OMI data is, that even in a long-term average from 2005 – 2008, there is no detection of the shipping SO_2 signal when integrating over the most busy shipping track of the world.

As for GOME-2, one can estimate the standard deviation of the OMI SO2 values over a clean region, and the result is comparable to that of GOME-2 with a standard deviation of about 1.7 DU. Considering the fact that on average, OMI pixels are about a factor of 10 smaller than GOME-2 pixels providing 10 measurements instead of one for the same area, the standard deviation of OMI SO2 data is about a factor of 3 better than that for GOME-2. As only 4 years of data have been used to avoid the problems with the row anomaly, the overall results for OMI are only about a factor of two better than those of GOME-2 (see Table 2).

Table 2: Estimated OMI SO2 standard deviations for different scenarios. All values are given for an AMF of 0.5 and assume a constant OMI signal to noise of 1.7 DU.

Scenario	Number of values	σ [10^{15} molec cm^{-2}]	σ [DU]
Single day	1	45	1.7
Single day, GOME-2 size	10	14.2	0.53
Month, all values, GOME-2 size	300	2.6	0.10
Month, clear-sky values, GOME-2 size	100	4.5	0.17
Year all values, GOME-2 size	3650	0.74	0.027
4 years, all values, GOME-2 size	14600	0.37	0.014
4 years, all values, integrated along track	262800	0.09	0.003

In summary, one could expect to see the signature of shipping SO_2 in a multi-year average at least when integrating along the shipping lane. However, this is not the case in operational OMI SO_2 data.

4. OMI IASB data

In addition to the operational OMI SO_2 data, there have recently been efforts to also develop scientific retrievals of SO_2 from OMI spectra. These retrievals are based on the DOAS approach as also applied for GOME-2, and as they use more spectral information, they have the potential to provide better signal to noise.

While these retrievals are still in the development phase, early results show that at least in multiannual averages, some SO_2 signals linked to ships can be seen (compare Figure 4.1). For example, there are enhanced SO_2 levels in the centre of the Red Sea which are clearly linked to the shipping lane seen in the NO_2 data. Outflow from land based sources (oil and gas refineries and flaring) complicate the separation of signals, but at least the feasibility of shipping SO_2 retrievals is demonstrated by these results.

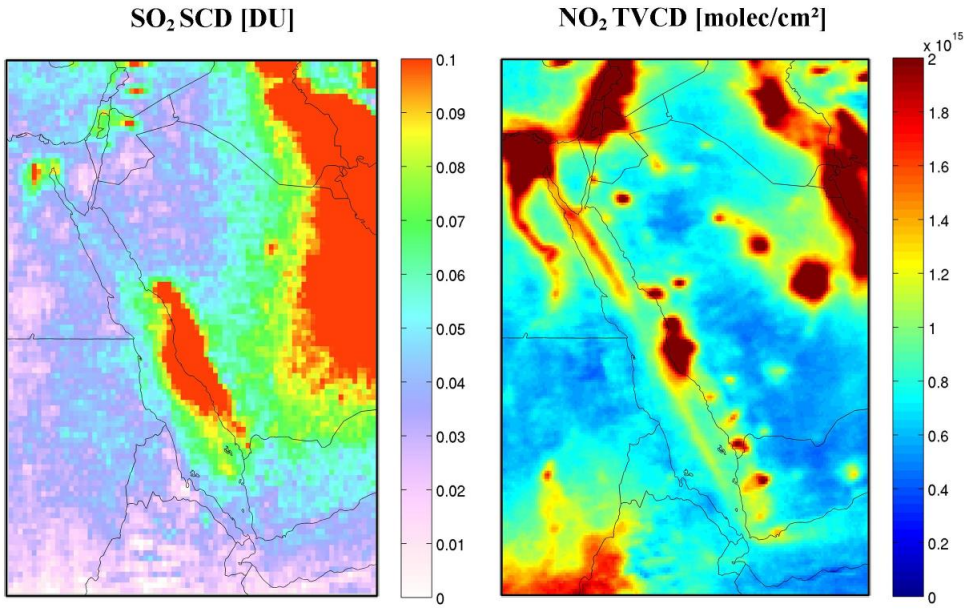

Figure 4.1: IASB Scientific OMI SO_2 retrieval over the Res Sea (left) compared to OMI tropospheric NO_2 (right). Data averaged over the time period 2004 – 2009 and only pixels having a cloud cover < 30% are included.

5. Potential of future missions

As discussed above, the expected signal from shipping SO_2 in satellite data is too small for noise levels of current instruments. While the size of the signal is limited by fundamental physical processes, there are some options to improve the detectability of such small BL SO_2 signals.

5.1. Reduced noise

The most important factor for better SO_2 retrievals is improved signal to noise of the spectra.

This can in general be achieved by

a) improving instrument throughput in the UV by reducing reflection and transmission losses and improving quantum efficiency of the detectors in the UV. In particular, optical degradation as observed in GOME-2 UV throughput should be minimised.
b) reducing photon shot noise by increasing the signal through larger entrance optics and larger detectors
c) reducing instrument noise by optimising dark signal, readout noise and any crosstalk issues.

Considering the high standard already realised in current instruments, the only obvious path to significantly better SO_2 retrievals are larger optics and detectors.

5.2. Increased number of measurements

In a similar way as increased optical throughput, a larger number of observations will improve signal to noise as long as the SNR of the individual observations remains the same. Thus combination of data from different instruments operating in parallel has the potential to improve SO_2 detectability.

Geostationary instruments such as S4 will provide several measurements per day, and if the small diurnal variation predicted by the model calculations shown in Section 2.2 is correct, these measurements can be combined to daily or weekly averages having better SO_2 signals.

For regional monitoring, UAVs or passive high altitude balloons or zeppelins would have a similar advantage as geostationary platforms with many measurements per day, and by limiting their observational area, much better spatial resolution could be realized. This in turn would further improve the detection of SO_2 as discussed in the next section.

5.3. Improved spatial resolution

Increased spatial resolution often improved detection of tropospheric signals for two reasons. First, the large spatial gradients in tropospheric constituent fields are better resolved in smaller ground pixels as less “dilution” by averaging is performed for peak values such as plumes from power plants. This effect is large for NO_2 but it is not clear how important it is for SO_2 which has a much longer atmospheric lifetime than NO_2 (up to a few days) and therefore is less well confined to the region of emission. This can be seen in the model results in Figure 2.1, where SO_2 does not appear to present spatial structures smaller than can resolved with current space instruments. It has to be kept in mind however that the spatial resolution of the

emission inventory and the chemistry transport model used in these calculations is approximately 10 km.

A second effect of improved spatial resolution is an increased number of cloud free observations as instrument resolution approaches typical cloud sizes in broken cloud conditions. By selecting observations looking between clouds a larger sensitivity to the boundary layer can be achieved but this is difficult to quantify.

5.4. Special viewing geometries

As is obvious from Figure 2.4, the surface reflectance plays an important role in the sensitivity of satellite observations to shipping SO_2. While oceans usually have very low albedo at the wavelengths used for SO_2 retrieval, observations under sun glint geometry have the potential to increase the reflection from the ocean surface to values of about 0.15, and thus the sensitivity to the BL. In current instruments the gain in sensitivity is offset by the much reduced number of observations over which one can average to improve signal to noise. However, future instruments could be operated in dedicated sun glint modes to maximize the number of sun glint observations over the oceans as is already done for GOSAT.

If a future instrument would have the ability for automatic active pointing during measurements, it could also be envisaged to increase the number of measurements over shipping regions at the expense of other regions and by avoiding cloudy pixels as much as possible.

5.5. Improved O_3 and SO_2 spectroscopy

As already discussed in Sec. 3, satellite SO_2 detection is mainly limited by the signal to noise of the measurements. However, for quantitative analysis, the spectroscopy of the interfering O_3 absorption and the temperature dependence of the SO_2 absorption cross-section are important factors.

The absorption cross-sections of O_3 and their temperature dependence are probably known with enough accuracy and the interference with the SO_2 retrieval which still is present in all SO_2 products is probably linked to a) the intrinsic correlation between the SO_2 and O_3 absorption cross-sections which cannot be removed, b) deficiencies in the knowledge of the instrument slit function which is important for the exact shape of the O_3 absorption and c) inaccuracies in the representation of the wavelength dependent effects of AMF and temperature dependence of the O_3 absorption for each specific atmospheric scenario (O_3 and T-profiles, viewing geometry).

Currently available measurements of the SO_2 cross-sections do not agree quantitatively on the temperature dependence and there is therefore a need for improved laboratory measurements of the temperature dependent SO_2 absorption cross-section.

Improvements on quantitative retrievals could thus come from better characterization and correction of slit function and radiative effects on ozone as well as a better knowledge of the temperature dependence of the SO_2 cross-section. Any effects on the detection of SO_2 shipping signals are however expected to be small.

6. Summary and Conclusions

CHIMERE simulations of SO_2 from ship emissions for the ship track between India and Indonesia which is the most visible in satellite NO_2 data predict relatively small SO_2 columns of 0.3 – 1.5x10^{15} molec cm^{-2}. As result of the longer atmospheric lifetime of SO_2, the ship track is less localised in SO_2 than in NO_2 fields, making detection more difficult. According to model results, changes in meteorology lead to a strong seasonal variation in shipping related SO_2 columns.

Strong Rayleigh scattering at the UV wavelengths used for the retrieval in combination with the dark surface limit the sensitivity of satellite observations of shipping SO_2 and lead to air mass factors of about 0.5, smaller by a factor of 4 than typical SO_2 AMFs for volcanic SO_2. The small AMFs in the shipping lane and larger AMFs elsewhere further complicate the unambiguous detection of shipping SO_2 and can potentially lead to false positive detection as AMF and assumed a priori ship signal are strongly correlated.

Analysis of the existing time series of GOME-2 and operational OMI SO_2 products show no indication of shipping signals, neither in long-term averages using all data, nor in averages limited to clear-sky scenes or the months with the largest model SO_2 columns. Only when integrating over the ship track area in the long-term global average of GOME-2 data, there is some hint of a shipping signal at the right latitude with about the magnitude predicted by the model, but it is questionable if this result is significant above the noise. In the IASB scientific OMI SO_2 product, the shipping lane in the Red Sea can be detected in a 5 year average, highlighting the potential of OMI data.

Analysis of the scatter of SO_2 vertical columns from GOME-2 data shows a standard deviation of about 40x10^{15} molec cm^{-2} over a clean tropical region in 2007 when applying AMFs appropriate for shipping SO_2. This value then deteriorates over the lifetime of the instrument. Based on the 2007 value and the CHIMERE simulations, it is expected that only the along-track integration of the long-term average will have a standard deviation smaller than the expected shipping signal, in agreement with the failure to identify a signal in the data. For OMI, the same calculations predict that SO_2 should just be detectable, in line with the first shipping SO_2 observations in OMI data reported by IASB.

In order to improve on this for future missions, the signal to noise of the measurements needs to be improved by a large factor. For example, for monthly detection to be possible, the SNR needs to be improved by about a factor of 10 which would require an increase in throughput and / or number of measurements by a factor of 100. Further increases would be necessary to move from detection to quantification of SO_2 emissions and their changes.

As all the calculations performed here were performed on the Indian Ocean area where observation conditions are very good (high sun, relatively low cloud frequency, high ship density) the conclusion of one order of magnitude missing in SNR is still optimistic for other regions such as European waters. It is therefore unrealistic to expect a contribution to the shipping SO_2 emission monitoring from satellites in the coming decade which goes beyond the detection of average values in the busiest shipping lanes.

7. References

Beirle, S., Platt, U., von Glasow, R., Wenig, M., and Wagner, T.: Estimate of nitrogen oxide emissions from shipping by satellite remote sensing, *Geophys. Res. Lett.*, 31, doi:10.1029/2004GL020312, 2004.

de Ruyter de Wildt, M., Eskes, H., and Boersma, K. F.: The global economic cycle and satellite-derived NO_2 trends over shipping lanes, *Geophys. Res., Lett*., 39, L01802, doi:10.1029/2011GL049541, 2012

Eisinger, M., and J. P. Burrows, Tropospheric Sulfur Dioxide observed by the ERS-2 GOME Instrument, *Geophys. Res. Lett.,* No. 25, pp. 4177-4180, 1998

Franke, K., Richter, A., Bovensmann, H., Eyring, V., Jöckel, P., and J. P. Burrows, Ship emitted NO_2 in the Indian Ocean: comparison of model results with satellite data, *Atmos. Chem. Phys.,* 9, 7289-7301, 2009

Ialongo, I., Hakkarainen, J., Hyttinen, N., Jalkanen, J.-P., Johansson, L., Boersma, F., Krotkov, N., and Tamminen, J.: Characterization of OMI tropospheric NO_2 over the Baltic Sea region, *Atmos. Chem. Phys. Discuss.,* 14, 2021-2042, doi:10.5194/acpd-14-2021-2014, 2014

Krotkov, N. A., Carn, S. A., Krueger, A. J., Bhartia, P. K., Yang, K., (2006), Band residual difference algorithm for retrieval of SO_2 from the Aura Ozone Monitoring Instrument (OMI), *IEEE Trans. Geosci. Remote Sensing, AURA Special Issue*, 44(5), 1259-1266, doi:10.1109/TGRS.2005.861932

Marbach, T., Beirle, S., Platt, U., Hoor, P., Wittrock, F., Richter, A., Vrekoussis, M., Grzegorski, M., Burrows, J. P., and Wagner, T., Satellite measurements of formaldehyde from shipping emissions, *Atmos. Chem. Phys.,* 9, 8223-8234, 2009

Richter, A., V. Eyring, J. P. Burrows, H. Bovensmann, A. Lauer, B. Sierk, and P. J. Crutzen, Satellite Measurements of NO_2 from International Shipping Emissions, *Geophys. Res. Lett.,* 31, L23110, doi:10.1029/2004GL020822, 2004

Richter, A., GOME-2 volcanic SO_2 algorithm theoretical basis document, Support to Aviation for Volcanic Ash Avoidance, Norw. Inst. for Air Res., Kjeller, Norway. (Available at http://savaa.nilu.no/PublicArchive/tabid/3207/Default.aspx.), 2009

Richter, A., Begoin, M., Hilboll, A., and Burrows, J. P.: An improved NO_2 retrieval for the GOME-2 satellite instrument, *Atmos. Meas. Tech.,* **4**, 1147-1159, doi:10.5194/amt-4-1147-2011, 2011

Rozanov, V., Rozanov, A., Kokhanovsky, A., and Burrows, J.: Radiative transfer through terrestrial atmosphere and ocean: software package SCIATRAN*, J. Quant. Spectrosc. Ra*., 133, 13–71, doi:10.1016/j.jqsrt.2013.07.004, 2014

Vinken, G. C. M., Boersma, K. F., van Donkelaar, A., and Zhang, L.: Constraints on ship NO_x emissions in Europe using GEOS-Chem and OMI satellite NO_2 observations, *Atmos. Chem. Phys. Discuss*., 13, 19351-19388, doi:10.5194/acpd-13-19351-2013, 2013

Yang, K., N. A. Krotkov, A. J. Krueger, S. A. Carn, P. K. Bhartia, and P. F. Levelt (2009), Improving retrieval of volcanic sulfur dioxide from backscattered UV satellite observations, *Geophys. Res. Lett.,* 36, L03102, doi:10.1029/2008GL036036.

Appendix A Meteorological and chemistry-transport modelling

A.1 Meteorological modelling

A.1.1 The WRF model

The numerical weather prediction model used in this study is the so-called Weather Research and Forecasting (WRF) model [Skamarock et al. 2008]. The WRF model is a state-of-the art regional atmosphere model developed by the National Center for Atmospheric Research (NCAR) in the United States in cooperation with many universities and other parties. The model is used by many institutes around the world, both for research and operational purposes. The model code is fully parallelised and can be used on hardware ranging from a single PC to the largest supercomputers.

The WRF model was written in a modular fashion, allowing flexible replacement and addition of different dynamics and parameterisations. The model has two ``dynamics cores'', one hydrostatic and one non-hydrostatic. At BMT ARGOSS the non-hydrostatic core is used, which can be used for a large range of spatial scales. For “real data” cases the model is typically applied to domains ranging from continental scale at resolutions of roughly 30 km down to domains with a resolution of 1 km. For “idealistic” cases the model can be used down to the scale of large-eddy simulations with resolutions of meters.

BMT ARGOSS uses the non-hydrostatic core of the model, allowing the simulation of small-scale non-stationary effects such as rapidly rising air under cumulus clouds. The model comes with a large number of physical parameterisation schemes. The model makes use of a surface layer scheme, a planetary boundary layer scheme, a cumulus parameterisation scheme for resolutions above 5 km, and a microphysics scheme allowing for the formation of ice, snow, graupel, and rain.

A.1.2 Model setup

WRF is a regional atmosphere model which means it cannot run without boundary conditions. Both the initial conditions and boundary conditions are supplied by NCEP FNL (Final Analysis) data. These data consist of analysed global fields into which most available meteorological measurements were assimilated. Historical final analysis data is available for the period 2000--2014.

The FNL data have a 1° x 1° spatial resolution and are available every six hours.

In this project runs have been made for 4 areas: Indian Ocean, eastern Mediterranean Sea, Bay of Biscay and Baltic. The domain setup for these areas is shown in figures A1 to A6. The target spatial resolution of the WRF domains is 9 km.

In order to make a smooth transition between the 1° x 1° resolution of the FNL data and the target resolution, the WRF model was set up with two nested domains: an outer domain with a 27 km resolution and an inner domain at 9 km resolution.

For each simulation a regular grid is used, defined on a Lambert conformal conical projection. The same grid is used for the CHIMERE runs. However, the outer 5 grid points of the WRF model grid are trimmed before using it.

The model was set up with a model top of 50 hPa and 31 vertical levels. The following physics parameterisations were used:

Table A1 Parameterisations used in the WRF simulations.

Parameterisation type	Name
Microphysics	Ferrier (new Eta) microphysics
Long-wave radiation	RRTM
Short-wave radiation	Dudhia
Surface layer	Monin-Obukhov
Land surface	Unified Noah
Urban	Not used
Boundary layer	YSU
Cumulus	Kain Fritsch (new Eta)

SRTM (Shuttle Radar Topography Mission) data were used to produce the topography for WRF and USGS (United States Geological Survey) data were used to produce the land-use maps.

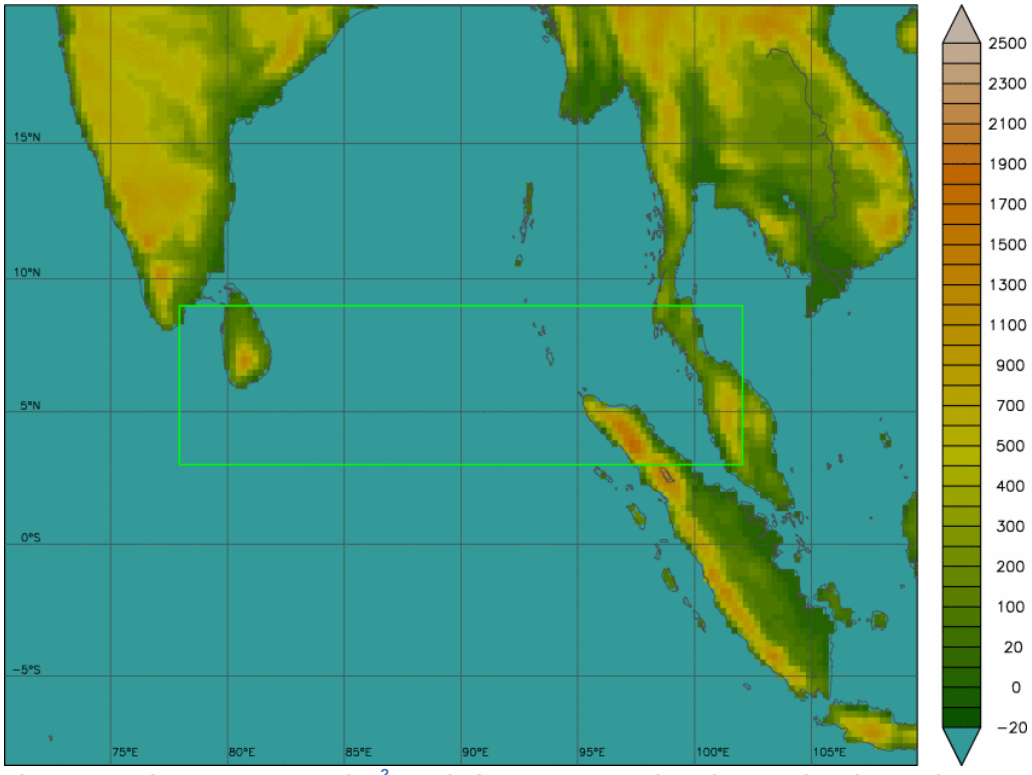

Figure A1 The outer, 27 x 27 km^2 resolution outer WRF domain covering the northern part of the Indian Ocean. The green rectangle marks the location of the 9 x 9 km^2 resolution inner domain.

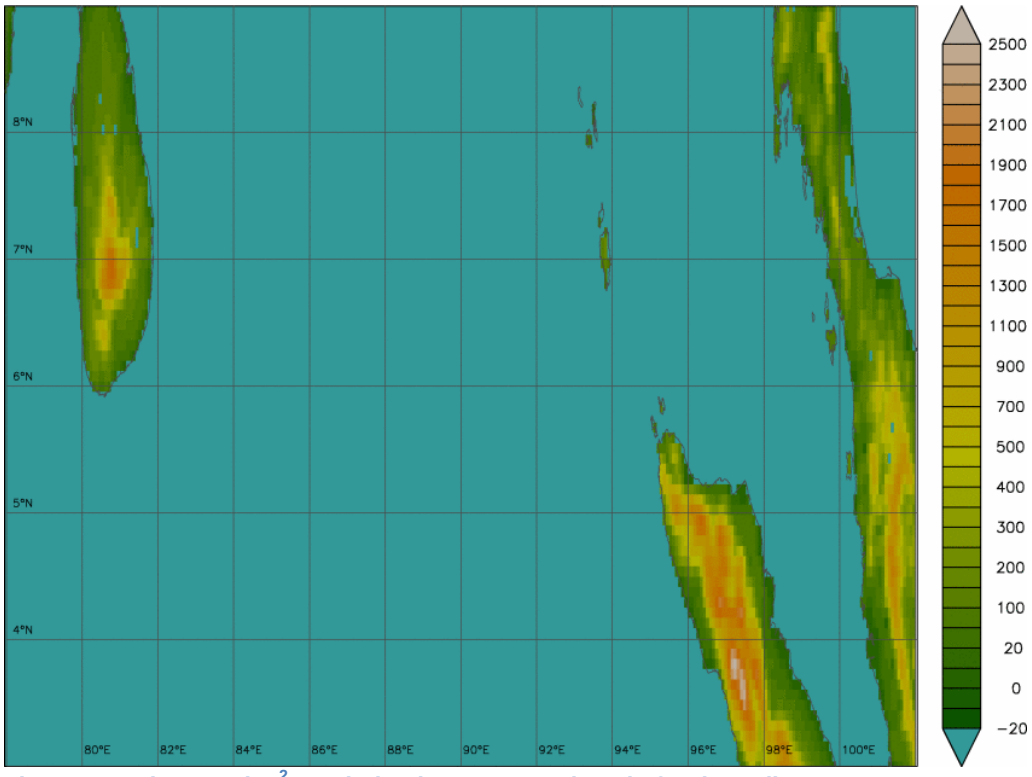

Figure A2 The 9 x 9 km^2 resolution inner, target domain for the Indian Ocean.

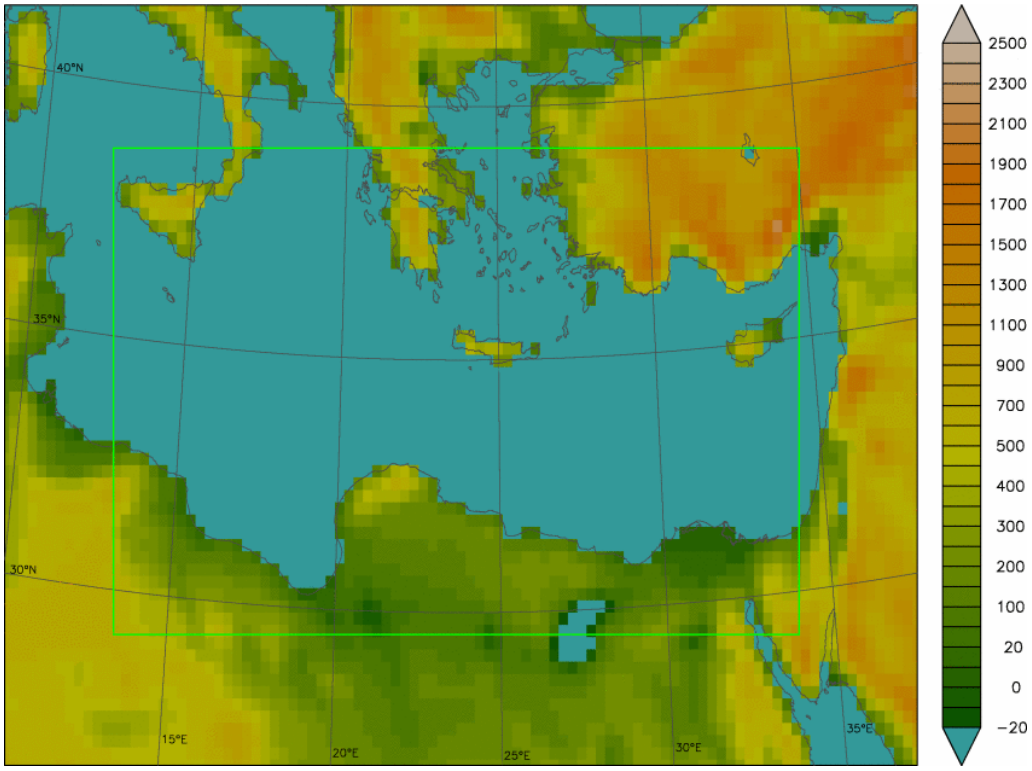

Figure A3 The outer, 27 x 27 km2 resolution outer WRF domain covering the eastern Mediterranean Sea. The green rectangle marks the location of the 9 x 9 km2 resolution inner domain.

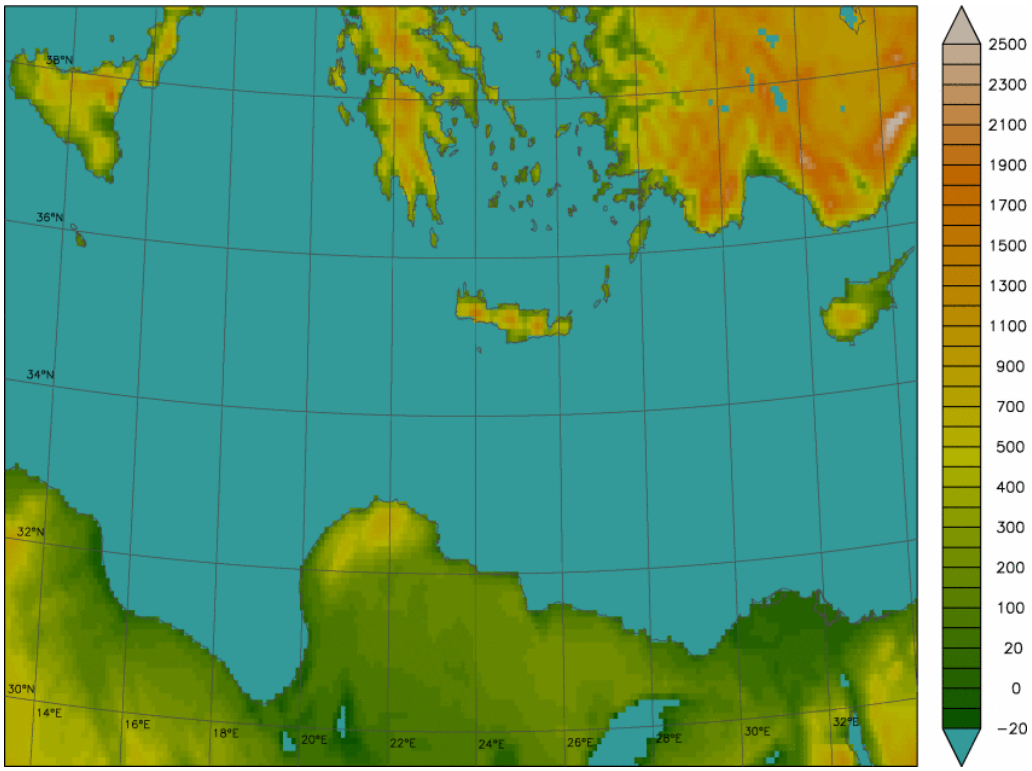

Figure A4 The 9 x 9 km2 resolution inner target domain for the eastern Mediterranean, covering the shipping lane from the Suez Canal to the southern tip of Sicily.

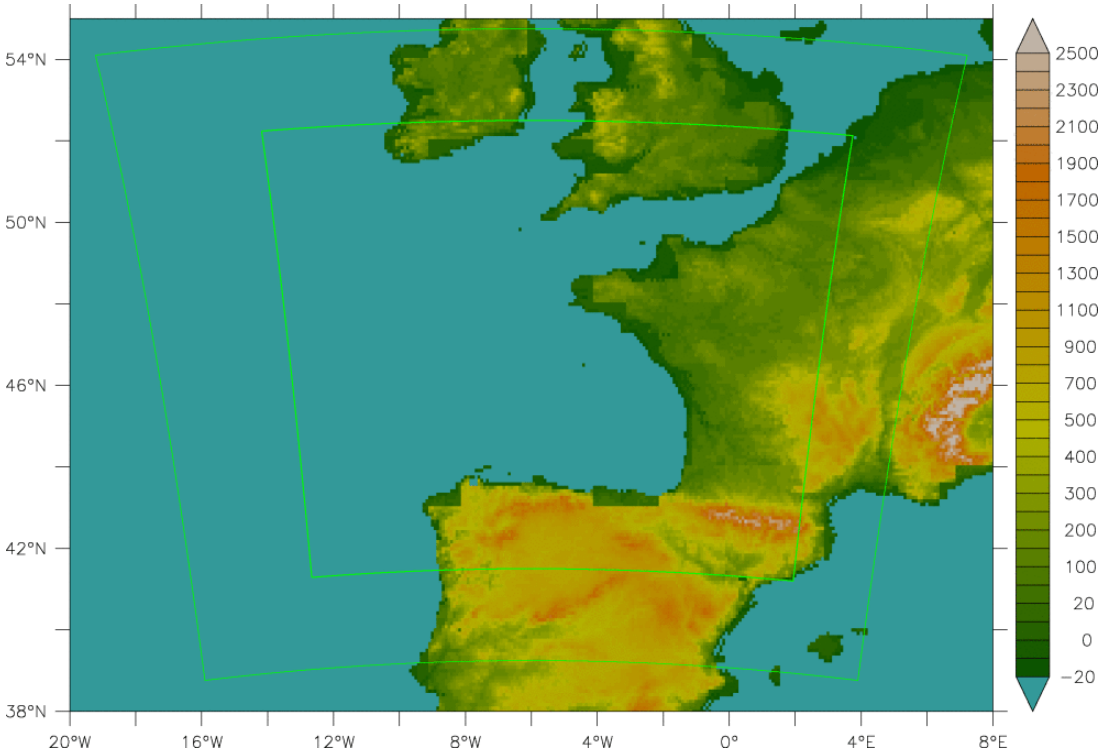

Figure A5 The WRF domain covering the Bay of Biscay. The outer green rectangle marks the 27 x 27 km^2 resolution WRF domain. The inner green rectangle marks the location of the 9 x 9 km^2 resolution domain.

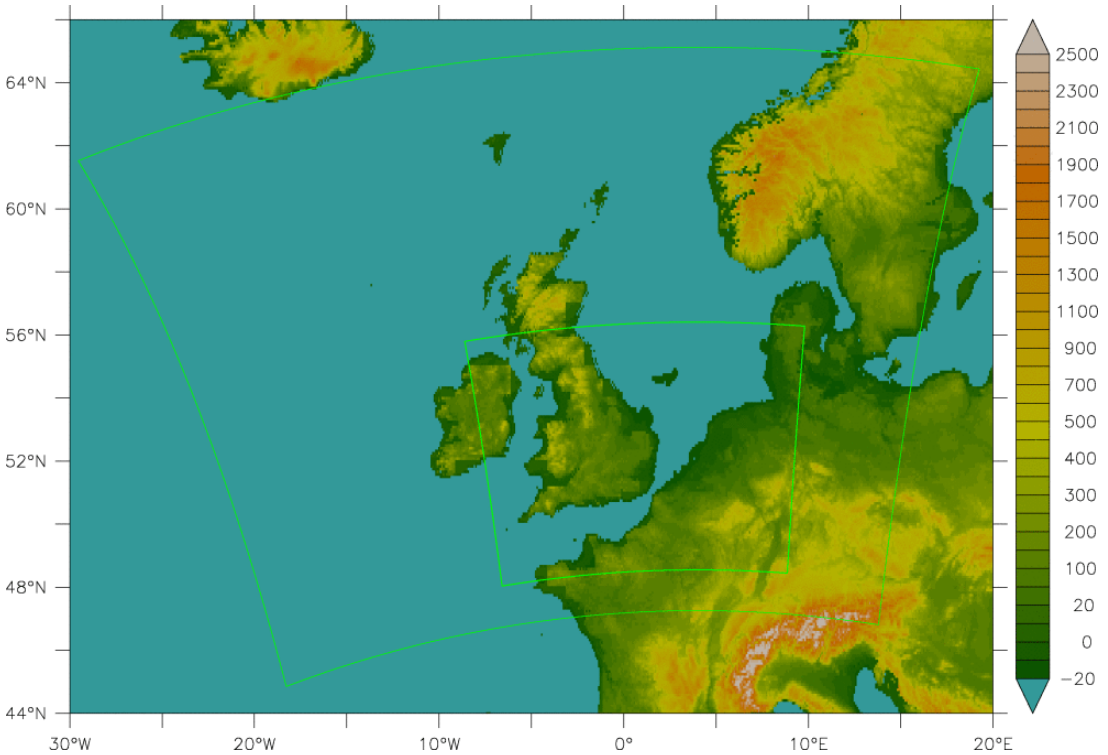

Figure A6 The WRF domain covering the North Sea. The outer green rectangle marks the 27 x 27 km2 resolution WRF domain. The inner green rectangle marks the location of the 9 x 9 km2 resolution domain.

A.1.3 Modelling strategy and output data

The WRF model was run with the domains shown in 0 for the year 2007. The model is run for a 48-hour period, and then it is re-initialised using NCEP FNL data. A six-hour long spin-up window is used before the start of each 48-hour period, overlapping with the previous simulation. Spin-up windows are discarded.
The model output consists of data of all major meteorological variables (incl. temperature, wind, pressure, humidity, geopotential height, the height of the planetary boundary layer) on the model grid. The data are available with a temporal resolution of one hour.
The primary weather model variables that are passed on to the chemistry-transport model are

- Temperature (3D)
- Pressure (3D)
- Humidity (3D)
- Wind speed and direction (3D)
- Incoming and outgoing radiation
- Precipitation
- Planetary boundary layer height

A.2 Air quality modelling

A.2.1 CHIMERE chemistry-transport model

The CHIMERE chemistry transport model is developed and maintained under the lead of researchers from the École Politechnique near Paris in France. The model is available under the GNU Public Licence. It can be downloaded from the Internet (see *http://www.lmd.polytechnique.fr/chimere*).

CHIMERE is capable of calculating the changes in air pollutant concentrations due to transport, turbulent diffusion, chemical transformations and deposition. The model requires several input data sets: information on meteorological conditions, boundary conditions (either from climatology or large-scale air quality models), land use data, biogenic emissions, and finally the locations and strengths of anthropogenic emission sources. The meteorological input data are generated in the SEARS project using the WRF model (see previous section).

Like the WRF model, CHIMERE can be applied on a wide variety of spatial scales from local (km or sub-km resolutions) to regional (hundred km resolution). The model can run with several vertical resolutions and with a wide range of complexity. It can use a simplified or a more complete set of chemical mechanisms; it can include or exclude aerosol and organic chemistry. There are also options to include dust uptake by wind, deep convection, urban heat island effects, etc. The temporal resolution of the model is typically one hour.

Table 2 provides a list of species whose emissions are required by CHIMERE. The model needs the average emissions for each species, per month, per day type (work days, Saturdays and Sundays), and for each hour of the day. The emission data is provided with 6 vertical layers representing pollutants emitted at various altitudes (road surface, chimneys).

Table A.2 Anthropogenic emissions, chemical species required by CHIMERE.

Chimére	Long name
APINEN	Alpha-pinene
BaP	Benzo(a)pyrene
BbF	Benzo(b)fluoranthene
BCAR	Primary black carbon
BkF	Benzo(k)fluoranthene
C_2H_4	Ethene
C_2H_5OH	Ethanol
C_2H_6	Ethane
C_3H_6	Propene
C_5H_8	Isoprene
CH_3CHO	Ocetaldehyde
CH_3COE	Methyl ethyl ketone
CH_3OH	Methanol
CH_4	Methane
CO	Carbon monoxide
H_2SO_4	Sulfuric acid
HCHO	Formaldehyde
HONO	Nitrous acid
NC_4H_{10}	n-Butane
NH_3	Ammonia
NO_2	Nitrogen dioxide
NO	Nitrogen monoxide
OCAR	Organic carbon
OXYL	o-Xylene
PPM_big	Primary PM (d > 10 µm)
PPM_coa	Primary PM (d = 2.5:10 µm)
PPM_fin	Primary PM (d < 2.5 µm)
SO_2	Sulfur dioxide
TMB	Trimethylbenzene
TOL	C_7H_8

CHIMERE is primarily designed to produce daily forecasts of ozone, aerosols, and other pollutants and to make long-term simulations (entire seasons or years) for emission control scenarios. The model can be used for the analysis of pollution events, research on various processes, scenario studies and forecasting and warning. Some of the application areas are the analysis of pollution problems in megacities, environmental assessments, health-impact studies, support to (governmental) organisations with their monitoring and reporting duties, short-term air quality forecasts for people with respiratory problems, etc.

A.2.2 CHIMERE pre-processor

The emissions are distributed over the model grid during a pre-processing step. The emission database which is readily available with the CHIMERE model is the EMEP (Co-operative programme for monitoring and evaluation of long-range transmission of air pollutants in Europe) database which has a 50 × 50 km^2 resolution. Emissions of carbonaceous aerosols are available from the LA CAPEDB (Laboratoire d'Áerologie database of emissions for carbonaceous aerosols) with a 0.25° × 0.25° resolution. The EMEP data contain yearly total emissions for a number of emission sectors and pollutants.

It is the task of the CHIMERE emission pre-processor to re-distribute the coarse EMEP emissions to the finer CHIMERE grids using a top-down approach. In broad lines, the pre-processor works as follows:

- Re-distribute the emissions in space based on land-use.
- Re-distribute the emissions in time using country-, sector-, and day-dependent profiles.
- Re-distribute the emissions to altitude levels using sector-dependent vertical profiles.
- Convert the EMEP species to the species needed by CHIMERE using a chemical aggregation/de-aggregation table.

During the land-use based spatial distribution, weights are assigned to the different land-use categories with cities having the largest and forests and water the smallest weight factors.

A.2.3 Emission databases

A chemistry transport model requires input from an emission database. The CHIMERE model was designed to use the EMEP data. However, the emissions in the EMEP database are not available for all project target areas and the 50 x 50 km^2 resolution is too coarse for modelling shipping lanes in the vicinity of land. The EDGAR emission database turned out to be more suitable. For application in this project this database was converted to become EMEP compatible, i.e. format was adapted and activity sectors were remapped.

EMEP emission database

The EMEP emissions database consists of gridded annual national emissions of sulphur oxide (SO_X), nitrogen oxides (NO_X=NO+NO_2), ammonia (NH_3), non-methane volatile organic compounds (NMVOC), carbon monoxide (CO), and particulates ($PM_{2.5}$, PM_{10}). These emissions are provided for 10 anthropogenic source-sectors denoted by so-called SNAP codes.

EDGAR emission database

The following species are available in the global EDGAR database: CH_4, CO, NH_3, NMVOC, NO_x, and SO_2.The data are available in the form of yearly averages, in units of km/m^2/s. The data are gridded and have a resolution of 0.1° x 0.1°. The data are split into IPCC activity sectors (one file per sector and species). The EDGAR v4.2 database was downloaded from: *http://edgar.jrc.ec.europa.eu/overview.php?v=42*.

To bring the EDGAR data in line with the EMEP data, the SO_2 emissions were converted to SO_X using a linear relation and emission values were scaled to change from kg/m^2/s to annual totals.

Redistribution of emissions based on land-use was not applied for the Edgar data, because the resolution is already good enough.

The annual mean NO_X emissions available in the EDGAR database are shown in figure A7. These emissions are pre-processed before entering the CHIMERE processing. The latter result is shown in figure A8. The two results are (almost) identical, confirming that EDGAR data was pre-processed correctly before going into CHIMERE. Figure A8 shows combined results of the 9 km and 27 km domains. Shipping lanes are clearly visible. Range of colour scales for figures A7 and A8 are chosen to enable viewing of shipping emissions. As a result colour scales saturate often for over land areas.

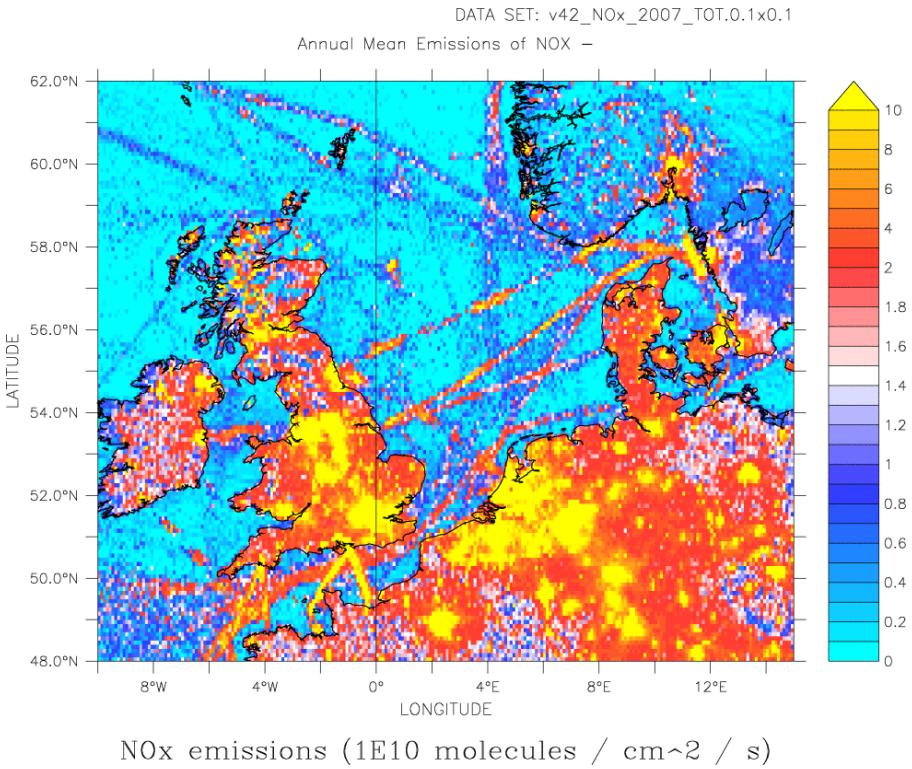

Figure A7 The annual NOX emissions according to the EDGAR database.

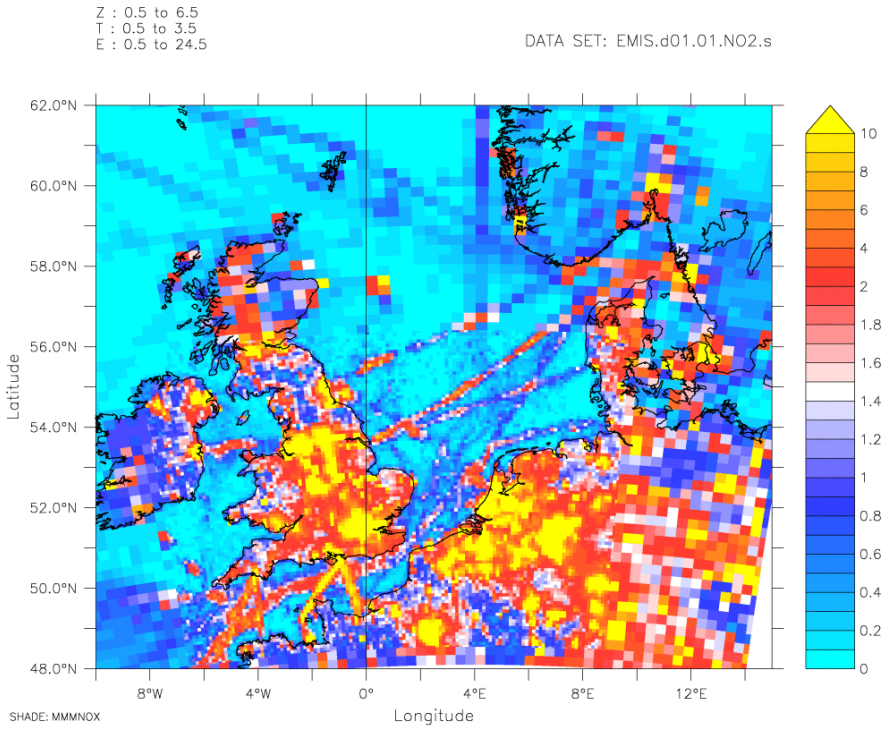

Figure A8 The NOX emissions after passing the CHIMERE pre-processor.

A.2.4 Correspondence between IPCC (EDGAR) and SNAP (EMEP) activity sectors

The EDGAR database uses the IPCC activity sectors which are not the same as the SNAP sectors used by EMEP. The pre-processing of the emissions in CHIMERE and in the BMT ARGOSS emission database is based on the SNAP sectors.

Main EMEP SNAP sectors are:

1. Combustion in energy and transformation industries
2. Non-industrial combustion plants
3. Combustion in manufacturing industry
4. Production processes
5. Extraction and distribution of fossil fuels and geothermal energy
6. Solvent use and other product use
7. Road transport
8. Other mobile sources and machinery
9. Waste treatment and disposal
10. Agriculture and forestry, land use and wood stock change

See also: http://www.emep.int/UniDoc/node7.html

Main EDGAR IPCC sectors are:

1. Energy
2. Industrial Processes
3. Solvents and other product use
4. Agriculture
5. Land use change and forestry
6. Waste
7. Other

See also: http://edgar.jrc.ec.europa.eu/methodology.php#12sou

The corresponding SNAP and IPCC sectors are presented in more detail in table A.3 [ref EMEP report 2013].

Table A.3 Correspondence between SNAP and IPCC activity sectors.

SNAP	SNAP name	IPCC	IPCC name
1	Combustion in energy and transformation industries	1A1	Energy industries
1.1, 1.2	Public power & District heating plants	1A1a	Public electricity and heat production
1.3	Petroleum refining plants	1A1b	Petroleum refining
1.4, 1.5	Solid fuel transformation plants & Coal mining, oil/gas extraction, pipeline compressors	1A1c	Manufacture of solid fuels and other energy industries
3	Combustion and manufacturing industry	1A2	Manufacturing industries and construction
8, 7, 1, 2	Other mobile sources and machinery & Road transport & Combustion and energy transformation industries & Non-industrial combustion plants	1A3	Transport
8.5	Airport and cruise traffic	1A3a	Civil aviation
7	Road transport	1A3b	Road transportation
8.2	Railways	1A3c	Railways
8.4, 8.3	Sea traffic & Inland waterways	1A3d	Navigation
8.10, 1.5	Other mobile sources and machinery & Pipeline compressors	1A3e	Other
2.1-2.3, 8.4, 8.6, 8.7, 8.9	Commercial and institutional plants & Residential plants & Plants in agriculture, forestry and aquaculture & National fishing & Agriculture & Forestry & Household and gardening	1A4	Other sectors
5.1, 4.2	Extraction and first treatment of solid fossil fuels & Coke oven (door leakage and extinction), solid smokeless fuel	1B1	Solid fuels
4.1, 5.2--5.6, 9.2	Processes in petrol industry & Extraction, first treatment and loading of liquid fossil fuels & Extraction, first treatment and loading of gaseous fossil fuels & Liquid fuel distribution (except gasoline) & Gasoline distribution & Gas distribution networks & Flaring in oil refinery and oil and gas extraction	1B2	Oil and natural gas
4.1, 5.2, 5.4, 5.5	Processes in petrol industry & Extraction, first treatment and loading of liquid fossil fuels & Liquid fuel distribution (except gasoline) & Gasoline distribution	1B2a	Oil
5.3, 5.6	Extraction, first treatment and loading of gaseous fossil fuels & Gas distribution networks	1B2b	Natural Gas
9.2	Flaring in oil refinery and oil and gas extraction	1B2c	Venting and flaring
4	Production processes	2	Industrial processes
4.6	Various	2A	Mineral products
4.4, 4.5	Various	2B	Chemical industry
4.6	Various	2D	Other production
4.8	Various	2E	Production of halocarbons and sulphur hexafluoride
6.1 -- 6.5	Various	2F	Consumption of halocarbons and sulphur hexafluoride
6.5.3	Refrigeration and air conditioning equipment using	2G	Other

	other products		
6.1 to 6.5	Various	3	Solvent and other product use
10.4	Various	4A	Enteric fermentation
10.5, 10.9	Various	4B	Manure management
10.1, 10.2	Rice field with/without fertilisers (e)	4C	Rice cultivation
10.1, 10.2, 11.5, 11.6	Cultures with fertilisers & Cultures without fertilisers & N_2O leakage of N into wetlands & N_2O leakage of N into waters	4D	Agricultural soils
	No SNAP sector allocated. Not relevant for Europe	4E	Prescribed burning of savannahs
10.3	Various	4F	Field burning of agricultural wastes
11.21	Various forests, grasslands/tundra and other	5A	Changes in forest and other woody biomass stocks
11.23	Various forests, grasslands/tundra and other	5C	Abandonment of managed lands
10.6, 11.24	Use of pesticides and limestone (CO_2 only) & CO_2 emissions from / or removals into soils	5D	CO_2 emissions and removals from soil
10???	Agriculture and forestry, land use and wood stock change	5F	Biomass burning
9.4	Waste disposal	6A	Solid waste disposal on land
9.10	Waste water treatment and latrines	6B	Waste water handling
9.2, 9.7, 9.9	Various forms of incineration	6C	Waste incineration
5.7	Geothermal energy extraction	7A	Other

A References

EMEP/EEA air pollutant emission inventory guidebook 2013, European Environment Agency report 2013. ISBN 978-92-9213-403-7

Skamarock, W. C., J. B. Klemp, J. Dudhia, D. O. Gill, D. M. Barker, M. G. Duda, X. Huang, W. Wang, and J. G. Powers, 2008: A description of the Advanced Research WRF Version 3. NCAR Tech Notes-475+STR